PAPER

Internal interface engineering in single-component hydrogels for interfacial solar evaporation

Yihan Shi,[a] Boyang Shi,[b] Shudi Mao, [ID] *[a] Xin Stella Zhang, [ID] [a] Casey Onggowarsito, [ID] [a] An Feng, [ID] [a] Guowei Wang, [ID] *[b] Dawei Su*[c] and Qiang Fu [ID] *[a]

Global water scarcity demands sustainable and high-efficiency freshwater production technologies. Interfacial solar evaporation (ISE) has emerged as a promising strategy; however, its broader application remains limited due to suboptimal evaporation rates, interfacial incompatibility among components, and performance degradation in complex wastewater environments. In this work, we introduce a single-component amphiphilic tetra-gel evaporator synthesized *via* a facile, efficient thiol–ene 'click' reaction between 4-arm polyethylene glycol thiol (tetra-PEG-SH) with α,ω-alkene-terminated poly(3-hexylthiophene) (alkene-P3HT-alkene). The resulting hydrogel undergoes spontaneous microscale phase separation, forming interwoven hydrophilic PEG and hydrophobic P3HT domains, which create dynamic internal air–water interfaces within the evaporator. Born–Oppenheimer molecular dynamics simulations confirm preferential hydration of PEG segments and persistent amphiphilic segregation, shedding light on the mechanism of internal interface formation. Under one-sun irradiation, the PEG-P3HT-based 2D evaporator achieves an exceptional evaporation rate of 6.24 kg m^{-2} h^{-1}, attributed to the enlarged and accessible internal evaporative surface. Moreover, it maintains high performance when treating challenging wastewater sources including lake sewage, oily wastewater, and laundry effluent. With its additive-free composition, salt-resilient structure, and consistent multi-cycle operation, PEG-P3HT presents a robust and innovative interfacial engineering platform for efficient solar-driven water purification.

Broader context

With merely ∼0.01% of Earth's water readily accessible as freshwater, over one-fifth of the global population faces escalating risks to health, food security, and ecosystems. Interfacial solar evaporation (ISE) has emerged as a promising and energy-efficient approach by confining heat to the water–air interface to enhance evaporation for freshwater production. However, existing two- and three-dimensional ISE designs restrict evaporation to external surfaces, prompting increasingly tall and inefficient structures in attempts to expand lateral surface area. In this study, we present a single-component amphiphilic tetra-gel evaporator that undergoes spontaneous microscale phase separation to create internal air–water interfaces. These embedded interfaces expand the active evaporative surface beyond the exterior geometry, enabling effectively volumetric evaporation. This approach not only addresses the long-standing issue of misleading projected-area normalization but also delivers significant gains in evaporation performance and material durability. Our findings introduce a transformative design principle that advances solar-driven water purification and opens new avenues for sustainable freshwater generation.

1. Introduction

Global water scarcity driven by population growth, industrial expansion, and climate change has exacerbated the demand for sustainable freshwater production technologies, particularly those adaptable to desalination, wastewater treatment, and resource recovery applications.[1–3] Interfacial solar evaporation (ISE) has emerged as a promising approach, utilizing solar energy to drive water evaporation at the air–water interface.[4,5] By localizing thermal energy precisely at this interface, ISE significantly enhances evaporation efficiency and minimizes energy loss, outperforming traditional bulk water distillation methods.

Previous advancements in the development of ISE systems have predominantly focused on optimizing two-dimensional (2D) hydrogel evaporators through strategic material selection and structural design.[6–9] Strategies included the incorporation of novel photothermal materials,[10] reduction of heat losses,[11] recycling of latent heat,[12] and lowering of evaporation enthalpy.[13] However, performance gains eventually plateaued due to the intrinsic limitations of planar geometries. Specifically, expanding the lateral dimensions of 2D evaporators often

[a]*Center for Technology in Water and Wastewater, School of Civil and Environmental Engineering, University of Technology Sydney, Ultimo, NSW 2007, Australia. E-mail: Qiang.Fu@uts.edu.au; shudi.mao@student.uts.edu.au*

[b]*Department of Macromolecular Science, Fudan University, Shanghai 200438, China. E-mail: gwwang@fudan.edu.cn*

[c]*Applied Chemistry & Environmental Science, School of Science, RMIT University, Melbourne, 3000 VIC, Australia. E-mail: dawei.su@rmit.edu.au*

results in central "dead zones" where vapor diffusion is hindered and convective transport is limited, ultimately diminishing overall evaporation efficiency.[14,15]

In response to the inherent constraints of planar evaporators,[16] recent research has pivoted toward the development of three-dimensional (3D) hydrogel evaporators, including conical arrays,[17,18] porous scaffolds,[19] and origami-inspired configurations.[20] These designs aim to increase lateral surface areas, enhance solar energy harvesting, and promote convective mass transport. Despite these advances, most 3D evaporators exhibit lower temperatures along their vertical evaporative surfaces.[21,22] While it can be argued that lower temperatures facilitate continuous ambient heat absorption, this counteracts the fundamental principle of ISE, which relies on localized heating at the evaporation interface. Moreover, the high water content and complex geometries of 3D hydrogels introduce mechanical stress, complicating fabrication and undermining long-term stability.

In parallel, carbon-based ISE systems, such as graphene oxide frameworks, doped porous carbon, and nanostructured composites have demonstrated excellent photothermal performance and structural versatility.[23–25] However, these systems typically rely on multicomponent architectures, which often lead to interfacial incompatibility and material non-uniformity. These limitations across both planar and composite platforms underscore the necessity of exploring alternative interfacial configurations.

Herein, we report a novel internal interfacial engineered, single-component[26] amphiphilic hydrogel, denoted as PEG-P3HT, synthesized *via* a thiol-ene 'click' reaction[27] between 4-arm poly(ethylene glycol) thiol (tetra-PEG-SH) and α,ω-alkene-terminated poly(3-hexylthiophene) (alkene-P3HT-alkene). The conjugated P3HT serves as an effective photothermal component, offering broad solar absorption of ∼85%. In contrast to conventional approaches that rely on blending photothermal material (PTM) additives into polymer networks, our PEG-P3HT hydrogel attains mechanical resilience through a covalently bonded single-component structure.[28] This design eliminates interfacial incompatibility between the PEG and P3HT segments, ensuring uniform stress distribution and enhanced durability. Notably, spontaneous microscale phase separation during solvent removal generates spatially correlated hydrophilic PEG microchannels and hydrophobic P3HT domains within the tetra-gel. During the ISE process, this unique architecture promotes the creation of dynamic internal air–water interfaces, enabling volumetric evaporation that surpasses the geometric surface constraints of conventional designs.

2. Results and discussion

As illustrated in Table S1, conventional 2D evaporators have equal sunlight projected area (PA) and evaporative area (EA). In contrast, 3D evaporators typically exhibit an increased EA due to their expanded surface geometry. Since water evaporation rates are commonly normalized to the PA in units of kg m^{-2} h^{-1}, the enhanced water mass loss resulting from the enlarged EA in 3D ISE systems is captured, but the actual increase in EA is not reflected in the calculation. As a result, 3D evaporators often report significantly higher evaporation rates compared to their 2D counterparts, despite the difference in effective evaporation surface area.

Building on this understanding, we propose a transformative conceptual shift: what if we could generate extensive internal air–water evaporation interfaces within the evaporator body, without impeding internal water transport pathways, to dramatically enhance evaporation performance? This concept challenges the prevailing design paradigm that confines evaporation to hydrogel surfaces or hydrophilic coatings. Instead, it introduces the concept of volumetric evaporation, whereby evaporation occurs at internally distributed air–water interfaces throughout the hydrogel matrix, thereby extending the effective interfacial area and more closely adhering to the core principles of ISE.

To achieve this, we designed and synthesized a novel single-component, amphiphilic tetra-gel evaporator incorporating hydrophobic P3HT and hydrophilic PEG segments. First, the alkene-P3HT-alkene (M_n = 6100 g mol^{-1}, Đ = 1.31) was synthesized *via* Grignard metathesis polymerization (GRIM),[29–31] yielding H-P3HT-Br with a number average molecular weight (M_n) of 5600 g mol^{-1} and a narrow dispersity of Đ = 1.16. It was sequentially modified through halogen–magnesium exchange, Vilsmeier–Haack formylation, and Grignard coupling with 3-butenylmagnesium bromide. The molecular weights, chemical structures and purity were confirmed by size-exclusion chromatography (SEC), proton nuclear magnetic resonance (^{1}H NMR), and matrix-assisted laser desorption/ionization time-of-flight mass spectrometry (MALDI-TOF MS), respectively. Complete synthetic procedures and characterization data are provided in SI Note S1 and Fig. S1–S6.

PEG-P3HT tetra-gel was then synthesized *via* a one-pot 'thiol-ene' reaction between tetra-PEG-SH and alkene-P3HT-alkene under a stoichiometric [SH]/[alkene] ratio (Fig. 1a). This approach enables the formation of a single-component, porous tetra-gel network with spontaneous phase separation of hydrophilic PEG and hydrophobic P3HT domains. To investigate the effect of amphiphilicity on evaporation performance, a hydrophilicity-enhanced variant (PEG-P3HT-PEGDA) was synthesized by replacing 50 mol% of the alkene-P3HT-alkene with poly(ethylene glycol) diacrylate (PEGDA), thereby increasing the proportion of hydrophilic PEG segments while maintaining a stoichiometric [SH]/[C=C] ratio. Additionally, a PEG-based hydrogel (PEG-MWCNT) was also prepared by crosslinking tetra-PEG-SH and PEGDA and incorporating 2 wt% multi-walled carbon nanotubes (MWCNT) as exogenous photothermal materials.

As shown in Fig. 1b and c, the PEG-P3HT tetra-gel shows a microporous network with pore sizes ranging from tens to hundreds of micrometers, ideal for capillary water transport and continuous vapor escape. Higher-magnification scanning electron microscopy (SEM) images reveal localized bulging along the pore walls, likely resulting from phase separation during solvent removal. These morphological irregularities enhance surface roughness compared to the PEG-P3HT-PEGDA and PEG-MWCNT hydrogels (Fig. S7). Correspondingly, PEG-
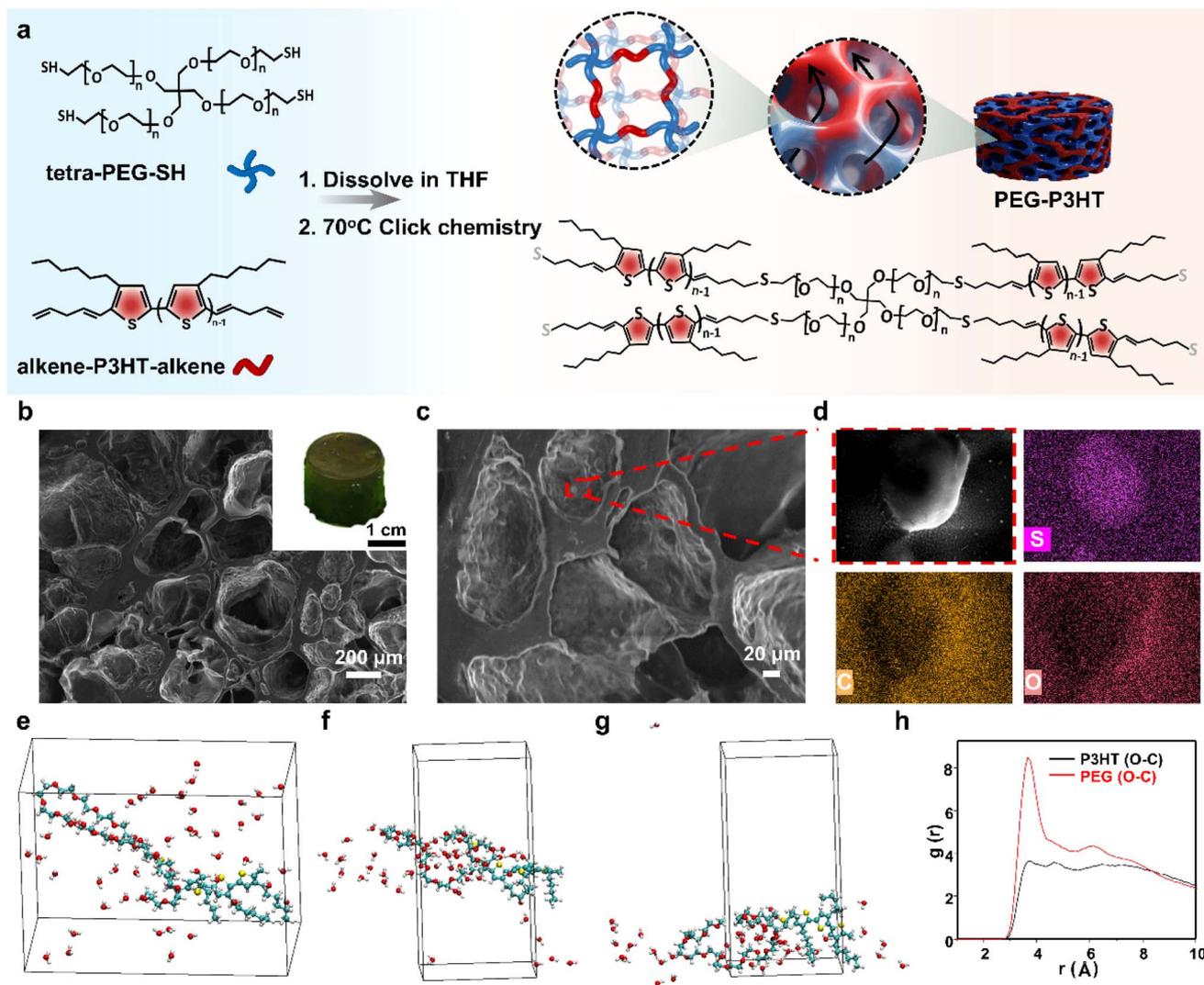
Fig. 1 Synthesis, morphology, and molecular simulation of PEG-P3HT hydrogels. (a) Thiol-ene 'click' reaction between tetra-PEG-SH and alkene-P3HT-alkene, yielding amphiphilic PEG-P3HT tetra-gel. (b) Low-magnification SEM image of the porous network; inset shows the hydrated gel. (c) High-resolution SEM of pore walls showing microscale bulges from phase separation. (d) EDS maps of C, O, and S confirming uniform distribution of PEG and P3HT segments. (e) Simulation setup showing three 3-hexyl thiophene units bearing long hydrophilic PEG chains (containing 18 EG units) surrounded by 50 water molecules in a $40 \times 30 \times 20$ Å^3 box. (f and g) BOMD snapshots at 34 ps and 100 ps showing water clustering around PEG and segregation of P3HT cores. (h) Radial distribution functions (RDFs) for O−C interactions showing preferential hydration near PEG chains at ∼3.6 Å.

P3HT shows a water uptake capacity of 6.75 g g^{-1}, ensuring effective hydration and rapid water transport (Fig. S8). The energy dispersive spectroscopy (EDS) elemental mapping (Fig. 1d) confirms the uniform distribution of sulfur (S), carbon (C), and oxygen (O), verifying the homogeneous incorporation of PEG and P3TH segments through the tetra-gel evaporator.

To elucidate the molecular forces behind the phase separation within the tetra-gel, we performed Born–Oppenheimer molecular dynamics (BOMD) simulations using CP2K (PBE/DZVP, 350 Ry cutoff, NVT at 300 K). A model system comprising three thiophene units, 18 ethylene glycol units (maintaining the same molar ratio of the two constituent units within the tetra-gel) and 50 water molecules was placed in a $40 \times 30 \times 20$ Å^3 cell and evolved for 100 ps (1 fs timestep; first 0.5 ps discarded as the pre-equilibrium) (Movie S1). As seen, within 34 ps, water overwhelmingly migrated to the hydrophilic PEG segments, while the 3-hexylthiophene units remained resolutely hydrophobic through 100 ps (Fig. 1e–g). Radial distribution functions revealed a pronounced O–C peak at ∼3.6 Å for the PEG tails *versus* the thiophene units (Fig. 1h), confirming preferential hydration of the PEG domains and robust phase separation. These atomistic insights underpin the tetra-gel's persistent hydrophobic/hydrophilic domains, which we later show is critical for volumetric evaporation.

Spectroscopic analyses provide clear evidence of successful preparation of single-component tetra-gel. In fourier transform infrared spectroscopy (FTIR) spectra (Fig. 2a), both PEG-P3HT and PEG-P3HT-PEGDA display broad O–H stretching bands
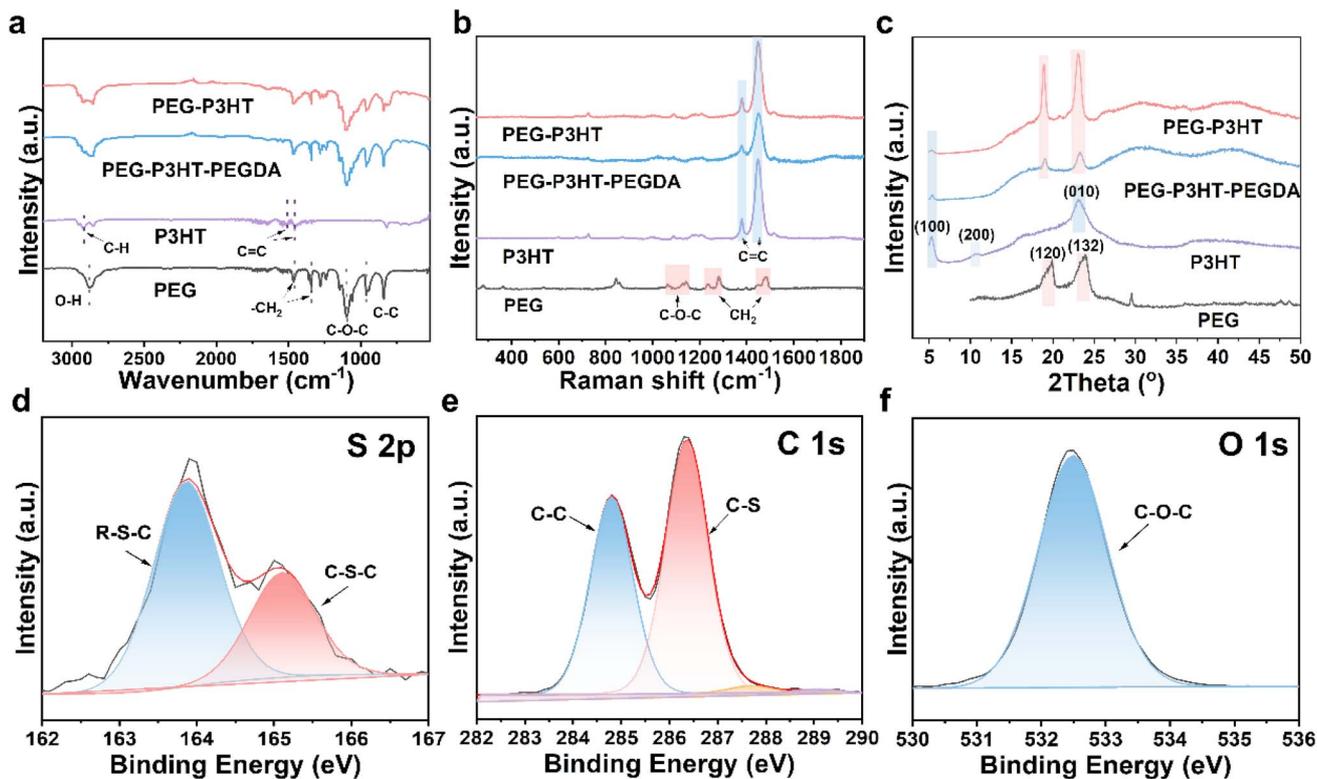
Fig. 2 Molecular characterization of PEG-P3HT hydrogels. (a–c) FTIR, Raman, and XRD spectra demonstrating successful incorporation of P3HT into the PEG-4SH network. (d–f) S 2p, C 1s, and O 1s XPS spectra of PEG-P3HT hydrogel.

around 3300 cm^{-1} and C–H stretching near 2920 cm^{-1}. Notably, the absorption bands at ~1100 cm^{-1} (C–O–C stretching) are prominent in the PEG-containing samples, while distinct peaks at 1450 and 1510 cm^{-1} in P3TH indicate cyclic thiophene units, which appear weakened in PEG-P3HT and PEG-P3HT-PEGDA due to network formation. Complementary Raman spectra (Fig. 2b) further validate the distinct chemical structures. PEG-P3HT retains thiophene-related bands at 1380 cm^{-1} and 1450 cm^{-1}, corresponding to symmetric and asymmetric C=C stretching vibrations of the thiophene rings, indicating preserved conjugation. In contrast, these peaks are attenuated in PEG-P3HT-PEGDA due to the reduced thiophene content, consistent with its more hydrophilic matrix and expected lower photothermal conversion efficiency. X-ray diffraction (XRD) patterns (Fig. 2c) reveal that both PEG-P3HT and PEG-P3HT-PEGDA hydrogels retain the P3HT lamellar (100) peak at $2\theta \approx$ 5.4° and the PEG (120) and (132) reflections at 19.0° and 23.2°, indicating that the polymerization process does not compromise the primary crystalline order of either component.

High-resolution X-ray photoelectron spectroscopy (XPS) analysis provides clear chemical evidence for thiol-ene click-mediated network formation. In the S 2p$_{3/2}$ spectrum (Fig. 2d), the appearance of a distinct peak at ~164 eV confirms the formation of C–S thioether bonds. In the C 1s spectrum (Fig. 2e), the significantly increased C–S/C–C intensity ratio in PEG-P3HT, compared to PEG-P3HT-PEGDA or pure PEG (Fig. S9 and S10), clearly confirms the successful incorporation of P3HT.

The O 1s signal at ~532.7 eV (Fig. 2f) reflects a uniform C–O–C ether environment, characteristic of a well-structured PEG backbone. Collectively, these key spectral features provide strong evidence for the efficient formation of a homogeneous amphiphilic tetra-PEG network *via* thiol-ene click chemistry.

UV-Vis-NIR spectroscopy was used to measure reflectance and transmittance of the hydrogel evaporators, from which solar absorptivity was calculated (Fig. 3a). The PEG-MWCNT control sample showed an absorptivity of 89%, resulting from the incorporated MWCNTs. PEG-P3HT and PEG-P3HT-PEGDA exhibited comparable broadband absorption of 85% and 80%, respectively, attributed to the intrinsic light-harvesting capacity of P3HT segments. The incorporation of P3HT through the thiol-ene reaction not only imparts photothermal performance comparable to that of carbon nanomaterials, but also mitigates the interfacial incompatibility typically observed between carbon materials and polymer matrices in conventional evaporators, thereby enhancing the structural integration of the tetra-gel network.

The photothermal response of PEG-P3HT and control samples were evaluated under one sun irradiation using a portable infrared camera in both dry and hydrated states (Fig. 3b and c). In the dry state, P3HT powder reached 57.8 °C, followed by PEG-P3HT (49.3 °C) and PEG-P3HT-PEGDA (44.6 °C), reflecting the strong intrinsic photothermal capacity of P3HT. When hydrated, all samples exhibited reduced temperature differentials due to two dominant energy redistribution
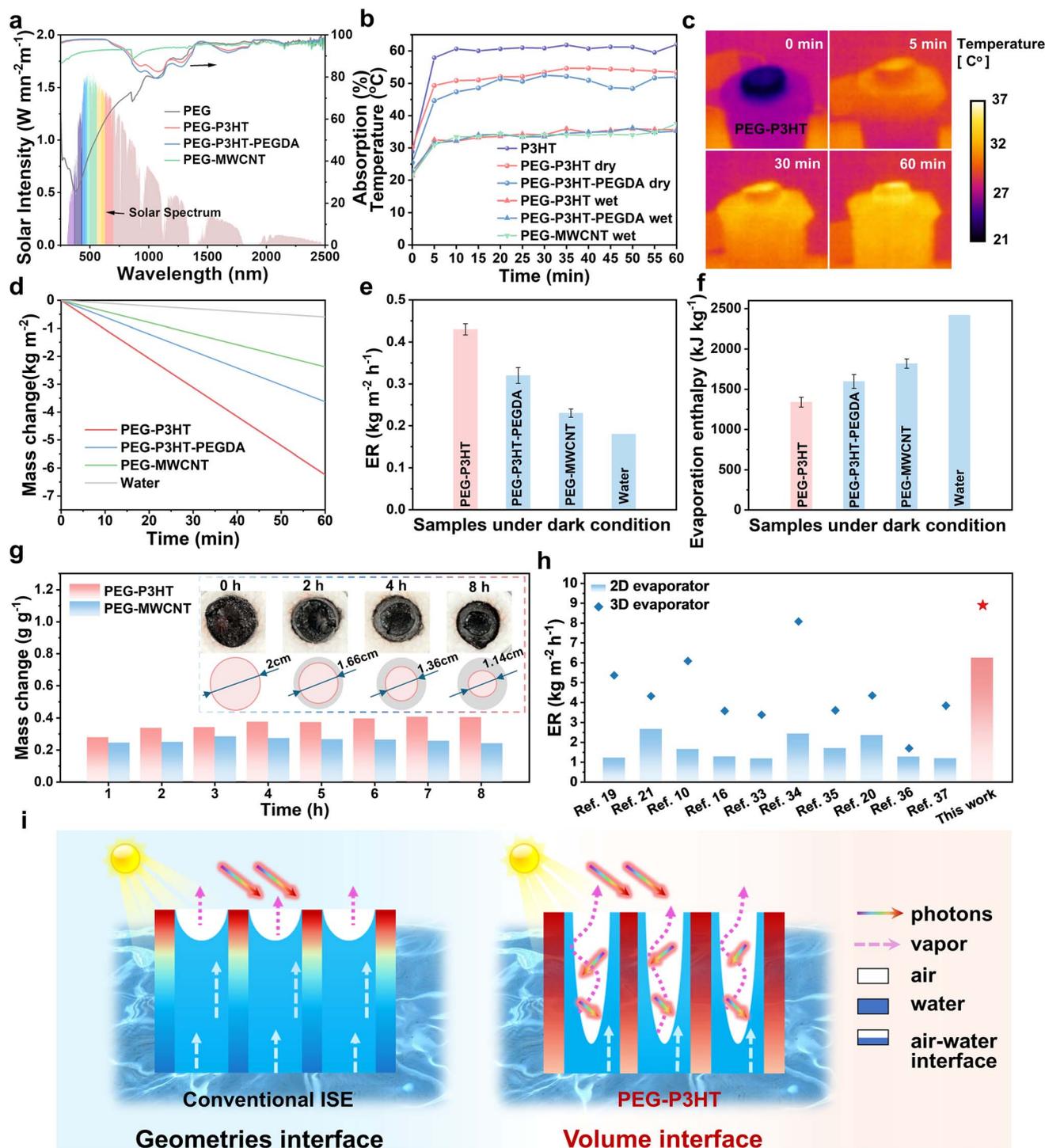
Fig. 3 Photothermal properties and evaporation performance. (a) UV-Vis-NIR spectra of PEG-P3HT, PEG-P3HT-PEGDA, and PEG-MWCNT showing broad solar absorption. (b) Surface temperature profiles under one-sun illumination indicating photothermal conversion. (c) IR images of PEG-P3HT over time under 1 sun illumination. (d) Mass loss *versus* time during solar evaporation (one sun). (e) Evaporation rates under dark conditions at 25 °C (baseline bulk water evaporation). (f) Effective vaporization enthalpies from DSC analysis. (g) Long-term gravimetric evaporation rates of PEG-P3HT and PEG-MWCNT, with PEG-P3HT showing stable ~0.38 g g^{-1} h^{-1} output. (h) Comparison of peak evaporation rates for PEG-P3HT and 3D PEG-P3HT against state-of-the-art 2D and corresponding 3D evaporators.[10,16,19–21,33–37] (i) Schematics comparing of conventional ISE and the volumetric interfacial network in PEG-P3HT.

processes: (i) heat transfer to the underlying water layer and (ii) latent heat consumption during water evaporation. PEG-P3HT demonstrated the most rapid thermal response, reaching

32.5 °C within the first 5 minutes, and all hydrated systems eventually equilibrated near 35 °C under one sun irradiation. This result indicates that the tetra-gel, with uniformly

distributed photothermal material P3HT, exhibits a rapid thermal response.

We then performed the evaporation tests using a house-built setup.[32] As expected, despite inevitable thermal losses, PEG-P3HT tetra-gel delivered an exceptional evaporation rate of 6.24 kg m^{-2} h^{-1}, nearly double that of the PEG-P3HT-PEGDA (3.63 kg m^{-2} h^{-1}) and almost three times that of PEG-MWCNT (2.38 kg m^{-2} h^{-1}) (Fig. 3d). Even in the dark, PEG-P3HT exhibits an evaporation rate of 0.43 kg m^{-2} h^{-1} at 25 °C, outperforming PEG-P3HT-PEGDA (0.32 kg m^{-2} h^{-1}), PEG-MWCNT (0.23 kg m^{-2} h^{-1}), and bulk water (0.18 kg m^{-2} h^{-1}) (Fig. 3e).

Differential scanning calorimetry (DSC) was employed to determine the equivalent enthalpy of water evaporation (Fig. S11). PEG-P3HT exhibited the lowest enthalpy of 1339 kJ kg^{-1}, representing approximately 55.3% of that of bulk water (2417 kJ kg^{-1}), indicating strong polymer–water interactions and a substantial amount of intermediate water content (Fig. 3f). In comparison, PEG-P3HT-PEGDA and PEG-MWCNT displayed higher enthalpies of 1596 and 1819 kJ kg^{-1}, respectively, in line with their relatively lower evaporation performance.

PEG-P3HT maintained stable and high ERs over 14 consecutive cycles under one sun irradiation (Fig. S12), confirming its long-term operational durability. Notably, gradual dimensional shrinkage was observed during extended operation, with the PEG-P3HT hydrogel diameter decreasing from 2 cm to 1.14 cm after 8 hours evaporation (Fig. S13 and S14). This volumetric contraction results in abnormally high evaporation rates (>19 kg m^{-2} h^{-1}) when calculated based on the projected area. To more accurately reflect the evaporation performance, the evaporation rate was normalized to the mass of the hydrated evaporator, directly linking the water loss to the evaporator's weight. As shown in Fig. 3g, the PEG-P3HT system consistently maintained an evaporation rate of approximately 0.38 L kg^{-1} h^{-1} over an 8 hour period, significantly outperforming its PEG-MWCNT counterpart.

In conventional 2D evaporators, evaporation occurs exclusively at the upper surface, representing the air–water interface, so the product of the evaporation rate $\dot{m}$ and the enthalpy of water evaporation ΔH is typically proportional to the effective evaporation area (EA). For the PEG-MWCNT evaporator, we measured the effective EA_1, $\dot{m}_1$ (Fig. 3d) and ΔH_1 (Fig. S11). For the PEG-P3HT evaporator, we measured the evaporation rate ($\dot{m}_2$) and enthalpy of evaporation (ΔH_2). Using eqn (1), we thus estimated the EA_2 of the PEG-P3HT system.

$$\frac{\dot{m}_1 \times \Delta H_1}{EA_1} = \frac{\dot{m}_2 \times \Delta H_2}{EA_2} \tag{1}$$

Calculations show that the PEG-P3HT tetra-gel provides 193% greater evaporation area than its PEG-MWCNT counterpart, directly validating its engineered internal interface mechanism.

Using the same synthetic procedure, we further fabricated a cylinder 3D PEG-P3HT evaporator with a diameter of 12.9 mm

and a height of 20 mm. This 3D evaporator exhibited an evaporation rate of 0.68 kg m^{-2} h^{-1} under dark conditions and 8.9 kg m^{-2} h^{-1} under one sun irradiation during eight-hour test (Fig. S15). Yet the geometric surface area increases by 170%, whereas the evaporation rate rises by 143%. This disparity pinpoints three coupled transport limitations: (i) capillary throttling—upward wicking periodically lags behind gravity, creating transient dry zones at the pillar apex; (ii) vapor crowding—elongated diffusion paths intensify concentration polarization, retarding mass release; and (iii) thermal stratification—multiple photon scattering suppresses IR loss but establishes a 3.4 °C vertical differences, focusing evaporation at hotspots instead of uniformly along the sidewall (Fig. S16).

To visualize the evaporation pathways *in situ*, we performed time-resolved optical microscopy on thin hydrogel slices. PEG-MWCNT rapidly saturates through capillary action, flooding within seconds and confining vapor release to its outer surface. In contrast, PEG-P3HT maintains dispersed and mobile menisci throughout its entire body, enabling sustained evaporation (Fig. S17). Notably, the contact-angle change is fully reversible: surface drying during steady evaporation increases θ to ~84.3°, while rehydration restores it to ~26.7° (Fig. S18). This dynamic shift reflects a self-induced increase in surface hydrophobicity that stabilizes microscale air pockets along P3HT-rich walls.

Fig. 3h (Table S2) compares the evaporation performance of our 2D PEG-P3HT evaporator with representative state-of-the-art 2D and 3D evaporators. As shown, the PEG-P3HT system demonstrates excellent performance, exceeding that of the reported 2D ISE systems and approaching the levels achieved by some 3D designs. It is worth noting that while several 3D evaporators report evaporation rates above 6 kg m^{-2} h^{-1}, their corresponding 2D counterparts, constructed from the same materials, often yield rates below 2.5 kg m^{-2} h^{-1}. This observation suggests that the improved performance in 3D architectures may largely result from the increased effective evaporation area, rather than intrinsic enhancements in thermal or water transport properties.

Collectively, these results provide compelling evidence that the exceptional evaporation performance of the PEG-P3HT evaporator stems from the synergistic triple functionality of its amphiphilic network (Fig. 3i). First, the uniformly distributed conjugated P3HT segments serve as highly efficient solar absorbers, rapidly converting incident light into localized heat. Unlike conventional ISE systems dependent on externally dispersed photothermal materials (*e.g.*, carbon/metallic nanomaterials), our design covalently integrates P3HT segments into a single-component network, enabling uniform volumetric heat generation *via* molecularly distributed solar-to-heat conversion sites. Simultaneously, the hydrophilic PEG matrix maintains continuous water pathways, ensuring sustained hydration and active internal evaporation. Third, spontaneous microphase separation between the two components gives rise to internal air–water interfaces, dramatically expanding the effective evaporative surface area within the tetra-gel matrix and enabling efficient vapor escape. By multiplying the active air–water interface far beyond the visible surface and leveraging dynamic wettability, this design achieves a record-high

evaporation flux, redefining the performance potential of hydrogel-based ISE systems.

Having demonstrated the outstanding evaporation performance of the PEG-P3HT evaporator resulting from its innovative design, we next carried out outdoor solar-driven evaporation and purification tests using diverse wastewater sources. Under natural sunlight in Sydney (April 3, 2025; 0.2–0.6 sun irradiation; Fig. 4a and b), a 2D PEG-P3HT device processed lake water over five daily cycles, yielding 19 L m^{-2} per day and demonstrating stable evaporation performance (Fig. 4c). In laboratory trials, PEG-P3HT achieved evaporation rates of 6.02 kg m^{-2} h^{-1} in methylene blue, 6.05 kg m^{-2} h^{-1} in methyl orange, 5.00 kg m^{-2} h^{-1} in lake sewage, 5.33 kg m^{-2} h^{-1} in oily

wastewater, and 5.56 kg m^{-2} h^{-1} in laundry effluent (Fig. S19), only modestly below the pure-water benchmark. As expected, ionic analysis of purified lake and seawater shows two to three orders-of-magnitude reductions in Na$^+$, K$^+$, Mg^{2+}, and Ca^{2+}, meeting the World Health Organization (WHO) drinking water criteria (Fig. 4d and e). The dye (i.e. MB, MO) removal efficiency was confirmed by UV-Vis spectroscopy, demonstrating the near-complete disappearance of characteristic absorption peaks (460 nm and 550 nm) and clear condensates (Fig. 4f and g). Microscopy validated the removal of algae, oil, and particulate matter from treated lake sewage, oily wastewater, and laundry effluent (Fig. 4h).
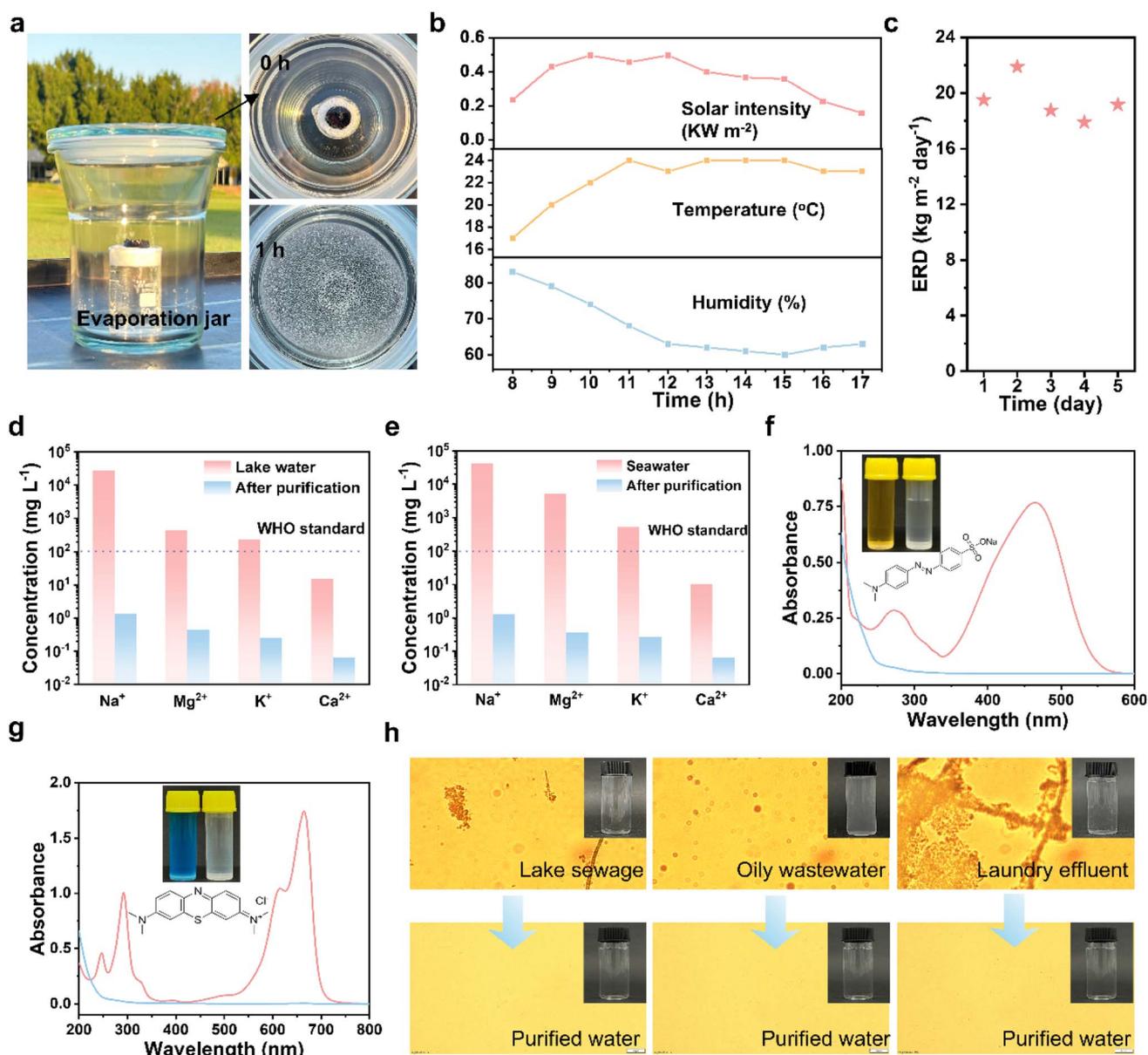

Fig. 4 PEG-P3HT for diverse water sources. (a) Outdoor ISE setup. (b) Solar irradiance, ambient temperature, and relative humidity during daylight (8:00–17:00). (c) Cumulative freshwater yield from lake water over five days. (d and e) Metal ion concentrations in treated lake water and seawater, reduced below WHO drinking-water limits. (f and g) UV-Vis spectra and photographic insets demonstrating removal of methyl orange (MO) and methylene blue (MB). (h) Photographs and microscopy images of raw and purified lake sewage, oily wastewater, and laundry effluent.

In saline environments, the amphiphilic architecture of PEG-P3HT confers excellent anti-fouling by preventing salt crystallization at the evaporation interface (Fig. S20). Hydrophobic P3HT domains block ions from migrating upward, so no visible salt crystals form on the surface even during long-term operation. However, the inherent hydrophobicity of P3HT impedes capillary-driven water transport, resulting in localized salt accumulation within the water channels. This leads to partial blockage at the pore entrances and ultimately reduces water flux to the evaporative interface (Fig. S21). Additionally, the presence of salt ions increases the evaporation enthalpy of water molecules, thereby limiting the amount of water that can be evaporated under a given photothermal conversion efficiency. As a result, the evaporation rate in high-salinity solutions is lower than that in pure water. Nevertheless, our PEG-P3HT evaporator consistently achieves higher evaporation rates than benchmark systems under identical saline conditions (Fig. S22 and Table S3), highlighting its salt-resilient, single-component design as a superior solution that balances anti-fouling capability with efficient photothermal performance. Together, these results highlight PEG-P3HT's versatility and durability for solar-driven purification across diverse, challenging water sources.

3. Conclusions

In summary, we report a single-component amphiphilic tetra-gel (PEG-P3HT) composed of hydrophobic P3HT and hydrophilic PEG segments, which undergo spontaneous phase separation within the porous network to form the internal air–water interfaces. Molecular dynamics simulations confirm rapid water uptake and sustained phase separation, supporting the proposed mechanism of volumetric evaporation. The resulting PEG-P3HT achieves a remarkable evaporation rate of 6.24 kg m^{-2} h^{-1} under standard conditions and consistently maintains rates above 5 kg m^{-2} h^{-1} when processing various source waters including lake sewage, oily wastewater, and laundry effluent. In outdoor field trials, a 2D PEG-P3HT evaporator processed lake water continuously for five days, yielding ~19 L m^{-2} per day with excellent stability. By harnessing internal evaporation pathways, this strategy has the potential to overcome the inherent geometric constraints of traditional evaporative surfaces and unlock new avenues for the development of high-performance interfacial solar evaporators.

4. Experimental section

4.1. Materials

Chemicals including poly(ethylene glycol) diacrylate (PEGDA, MW = 6 kDa), benzoyl peroxide (BPO), tetrahydrofuran (THF), multi-walled carbon nanotube (MWCNT), and sodium dodecyl sulfate (SDS) were supplied by Sigma-Aldrich. 4-Arm poly(ethylene glycol) thiol (tetra-PEG-SH, MW = 20 kDa) was purchased from Jenkem Technology, USA. All the materials and chemicals were used as received. α,ω-Alkene terminated poly(3-hexylthiophene) was prepared following the procedure detailed in Note S1.

4.2. Fabrication of PEG-P3HT, PEG-P3HT-PEGDA, and PEG-MWCNT

For PEG-P3HT preparation, tetra-PEG-SH and alkene-P3HT-alkene with a [SH]/[alkene] ratio of 1 : 1 were dissolved in THF and sonicated for complete dissolution and homogeneous mixing to prepare 10 wt% precursor. BPO was then added at a concentration of 3 wt% relative to the total precursor mass. The mixture was heated in an oil bath at 70 °C for 6 hours to perform thiol-ene reaction. The resulting tetra-gel underwent solvent exchange by immersion in deionized water, followed by freezing at −18 °C overnight. The gel was then thawed in deionized water until fully saturated to form the PEG-P3HT hydrogel. For PEG-P3HT-PEGDA preparation, 50 mol% of the alkene-P3HT-alkene was substituted with poly(ethylene glycol) diacrylate (PEGDA).

For PEG-MWCNT, 100 mg of tetra-PEG-SH and 60 mg of PEGDA was dissolved in 1.6 mL of THF and sonicated to obtain a 10 wt% solution. MWCNTs were added at 2 wt% relative to the PEG mass and dispersed uniformly. BPO was incorporated at a 3 wt% loading relative to the total precursor mass. The mixture was subjected to oil bath at 70 °C for 6 hours. The resulting product underwent solvent exchange by immersion in deionized water, followed by freezing at −18 °C overnight, and was then thawed in deionized water until fully saturated.

4.3. Characterization

The morphology of evaporators was observed using a Zeiss EVO scanning electron microscope (SEM) with EDS detector. The chemical state of Carbon (C), Oxygen (O) and Sulfur (S) was determined using an ESCAB 250xi X-ray photoelectron spectroscope (XPS). The Raman spectrum was analyzed using a Renishaw Raman spectrometer (Gloucestershire, UK), operating in the wavelength range of 200–2000 nm. X-ray diffraction (XRD) analysis were performed on a Bruker D8 Discover diffractometer with a Cu Kα source. Phase identification was conducted with the ICDD-PDF-4 database and crystal structure analysis using Topas software. Fourier transform infrared spectroscopy (FT-IR) was performed using a Thermo Scientific Nicolet 6700 spectrometer (USA). Optical contact angle measurements and analysis were conducted using a contact angle meter (OCA100, Germany. A volume of 3 μl fresh pure water was dispersed at three different sample regions. Reflection (R) and Transmission (T) spectra were collected using an Ultraviolet-visible-infrared (UV-Vis-NIR) spectrophotometer (Perkin Elmber Lambda 950, USA) operating in the wavelength range of 300–2500 nm. The solar absorption (A) was calculated by $A = 1 - R - T$. The vaporization enthalpy of hydrogels was measured on a differential scanning calorimeter (DSC, SDT Q600 V20.9, USA). The evaporation enthalpy was calculated based on eqn (2):

$$\Delta H_{equ} = \int_{t_0}^{t} \dot{q} dt \tag{2}$$

where t is time, and $\dot{q}$ is the heat flux characterized using DSC.

The freeze-dried sample (m_0) was submerged in deionized water, removed at 5 minute intervals, blotted with filter paper,

and reweighed (m_s) until equilibrium was reached. The saturated water content was then calculated using eqn (3):

$$Q_s = \frac{m_s - m_0}{m_0} \tag{3}$$

4.4. Indoor evaporation tests

Solar steam generation experiments were conducted using a solar light simulator (NBeT HSX-F3000 xenon light source, China), and the power density of the irradiation was measured with a compact power meter (PM100D, Thorlabs, Germany) and a thermal power sensor (S405C, Thorlabs, Germany). The temperature of both the hydrogel surface and bulk water was recorded using an IR camera (Fluke PTi120, USA). Water mass change was monitored with an electronic balance (OHAUS Pioneer IC-PX 124, China) with a precision of 0.001 g. The samples were placed on the water surface in a glass vessel, and EPE foam covered any unoccupied areas. The samples were then irradiated under one sun illumination (1 kW m^{-2}). The laboratory was maintained at approximately 25 °C, and the evaporation rate was measured in 2 h under steady-state conditions. The water evaporation rate was calculated by eqn (4):

$$\dot{m} = \frac{\mathrm{d}m}{S\mathrm{d}t} \tag{4}$$

where m is the mass of evaporated water, S is the illuminated area, and $\dot{m}$ is evaporation rate.

For *in situ* visualization of evaporation dynamics, hydrogel samples were cryo-sectioned into ~200 μm-thick slices, fully saturated in water, and mounted on glass slides. Evaporation was observed under the same ambient conditions (25 °C, 40% RH) to slow drying and enable clear tracking of internal structural changes. Time-resolved optical microscopy images of PEG-P3HT and PEG-MWCNT were recorded simultaneously using an optical microscope (Olympus, BX41) at 10× magnification.

4.5. Outdoor evaporation tests

Seawater, lake sewage, and laundry effluent were collected locally. Peanut oil and water (1 : 99 v/v) with 0.2 mg mL^{-1} SDS were stirred 1 h and ultrasonicated for 15 min to simulate the oily wastewater. The outdoor evaporation experiments were conducted using a transparent jar under natural sunlight irradiation on the Booralee Park (33.94°S, 151.20°E) in Sydney, from 8:00 and 17:00. The salinity and concentrations of ions before and after solar desalination were analyzed by an inductively coupled plasma emission spectrometer (ICP-MS, Agilent 7900, USA). The optical images of diverse water sources were taken by microscope (Olympus, BX41).

4.6. Born–Oppenheimer Molecular Dynamics (BOMD) simulations

Born–Oppenheimer Molecular Dynamics (BOMD) simulations were conducted using the CP2K package.[38–40] The calculations were carried out using density functional theory (DFT) with the spin-polarised gradient corrected functional of PBE as well. The wave functions were expanded in a molecularly optimised double-ζ Gaussian basis set to minimise basis set superposition errors. The Gaussian basis set was double-with one set of polarisation functions (DZVP).[41] An additional auxiliary plane wave basis of 350 Ry energy cutoff was used to calculate the electrostatic energy terms. The Γ-point approximation was employed for Brillouin Zone integration. Canonical ensemble (NVT) conditions were imposed by a Nosé–Hoover thermostat with a target temperature of 300 K. The MD time step is set to 1 fs. For all the MD trajectories, the initial ~0.5 ps was regarded as the equilibration period, followed by production periods. To investigate the interaction between water molecules and amphiphilic polymer block, 3 thiophene units and 18 EG units were established together with 50 water molecules in a 40 × 30 × 20 Å^3 unit cell.

Author contributions

Y. S. designed the experiments and carried out this project. Y. S., B. S., S. M., X. Z., A. F. and C. O. performed the experiments and characterization. D. S. conducted the BOMD simulation. G. W. revised the manuscript. Q. F. conceived the idea, supervised this project, and revised the manuscript.

Conflicts of interest

The authors declare no competing interests.

Data availability

The data supporting this article have been included as part of the SI.

Supplementary information includes synthetic procedures, material characterization data, evaporation performance figures and tables, and a simulation video. See DOI: **https://doi.org/10.1039/d5el00097a**.

Acknowledgements

References

1 C. He, Z. Liu, J. Wu, X. Pan, Z. Fang, J. Li and B. A. Bryan, *Nat. Commun.*, 2021, **12**, 4667.

2 M. Kummu, J. H. A. Guillaume, H. de Moel, S. Eisner, M. Floerke, M. Porkka, S. Siebert, T. I. E. Veldkamp and P. J. Ward, *Sci. Rep.*, 2016, **6**, 38495.

3 M. M. Mekonnen and A. Y. Hoekstra, *Sci. Adv.*, 2016, **2**, e1500323.

4 Y. Shi, A. Feng, S. Mao, C. Onggowarsito, X. Stella Zhang, W. Guo and Q. Fu, *Chem. Eng. J.*, 2024, **492**, 152303.

5 C. Onggowarsito, S. Mao, X. S. Zhang, A. Feng, H. Xu and Q. Fu, *Energy Environ. Sci.*, 2024, **17**, 2088–2099.

6 C. Li, S. Cao, J. Lutzki, J. Yang, T. Konegger, F. Kleitz and A. Thomas, *J. Am. Chem. Soc.*, 2022, **144**, 3083–3090.

7 Z. Huang, Y. H. Luo, W. Y. Geng, Y. Wan, S. Li and C. S. Lee, *Small Methods*, 2021, **5**, e2100036.

8 C. Lei, W. Guan, Y. Guo, W. Shi, Y. Wang, K. P. Johnston and G. Yu, *Angew Chem., Int. Ed. Engl.*, 2022, **61**, e202208487.

9 Y. Lu, D. Fan, Y. Wang, H. Xu, C. Lu and X. Yang, *ACS Nano*, 2021, **15**, 10366–10376.

10 B. Yang, Z. Zhang, P. Liu, X. Fu, J. Wang, Y. Cao, R. Tang, X. Du, W. Chen, S. Li, H. Yan, Z. Li, X. Zhao, G. Qin, X. Q. Chen and L. Zuo, *Nature*, 2023, **622**, 499–506.

11 X. Zhao, H. Zhang, K. Y. Chan, X. Huang, Y. Yang and X. Shen, *Nano-Micro Lett.*, 2024, **16**, 222.

12 C. Onggowarsito, S. Zhang, Y. Shi, S. Mao, A. Feng, G. Martins, Z. Shao, E. H. H. Wong, W. Guo and Q. Fu, *Chem. Eng. J.*, 2025, **513**, 162838.

13 Z. Yu, R. Gu, Y. Tian, P. Xie, B. Jin and S. Cheng, *Adv. Funct. Mater.*, 2022, **32**, 2108586.

14 T. Gao, Y. Wang, X. Wu, P. Wu, X. Yang, Q. Li, Z. Zhang, D. Zhang, G. Owens and H. Xu, *Sci. Bull.*, 2022, **67**, 1572–1580.

15 Y. Guo, X. Zhao, F. Zhao, Z. Jiao, X. Zhou and G. Yu, *Energy Environ. Sci.*, 2020, **13**, 2087–2095.

16 H. Liu and W. Zhai, *Adv. Funct. Mater.*, 2025, 202417169.

17 Z. Huang, J. Wei, Y. Wan, P. Li, J. Yu, J. Dong, S. Wang, S. Li and C. S. Lee, *Small*, 2021, **17**, e2101487.

18 L. Wu, Z. Dong, Z. Cai, T. Ganapathy, N. X. Fang, C. Li, C. Yu, Y. Zhang and Y. Song, *Nat. Commun.*, 2020, **11**, 521.

19 Y. Chen, J. Hao, J. Xu, Z. Hu, H. Bao and H. Xu, *Small*, 2023, **19**, e2303908.

20 Y. Wang, X. Wu, T. Gao, Y. Lu, X. Yang, G. Y. Chen, G. Owens and H. Xu, *Nano Energy*, 2021, **79**, 105477.

21 X. Wu, Z. Wu, Y. Wang, T. Gao, Q. Li and H. Xu, *Adv. Sci.*, 2021, **8**, 2002501.

22 X. Li, J. Li, J. Lu, N. Xu, C. Chen, X. Min, B. Zhu, H. Li, L. Zhou, S. Zhu, T. Zhang and J. Zhu, *Joule*, 2018, **2**, 1331–1338.

23 Y. Ma, X. Meng, K. Li, L. Zhang, Y. Du, X. Cai and J. Qiu, *ACS Catal.*, 2023, **13**, 1290–1298.

24 X. Zhao, X. Meng, H. Zou, Z. Wang, Y. Du, Y. Shao, J. Qi and J. Qiu, *Adv. Funct. Mater.*, 2022, **33**, 2209207.

25 H. Zou, X. Meng, X. Zhao and J. Qiu, *Adv. Mater.*, 2023, **35**, e2207262.

26 D. Mawad, E. Stewart, D. L. Officer, T. Romeo, P. Wagner, K. Wagner and G. G. Wallace, *Adv. Funct. Mater.*, 2012, **22**, 2692–2699.

27 C. E. Hoyle and C. N. Bowman, *Angew. Chem., Int. Ed.*, 2010, **49**, 1540–1573.

28 S. Guo, S. Zhang, H. Li, S. Liu, J. J. Koh, M. Zhou, Z. Sun, Y. Liu, H. Qu, Z. Yu, Y. Zhang, L. Yang, W. Chen, C. He, C. Lee, D. Mao, S. K. Ravi, Y. Lai and S. C. Tan, *Matter*, 2025, **8**, 101785.

29 M. Jeffries-El, G. Sauvé and R. D. McCullough, *Macromolecules*, 2005, **38**, 10346–10352.

30 H. Lim, C.-Y. Chao and W.-F. Su, *Macromolecules*, 2015, **48**, 3269–3281.

31 A. Yokoyama, R. Miyakoshi and T. Yokozawa, *Macromolecules*, 2004, **37**, 1169–1171.

32 Q. Xiong, D. Wang, B. Shao, H. Yu, X. Wu, Y. Lu, X. Yang and H. Xu, *Adv. Funct. Mater.*, 2025, **35**, 2409257.

33 L. Chen, J. Ren, J. Gong, J. Qu and R. Niu, *Chem. Eng. J.*, 2023, **454**, 140383.

34 L. Sun, X. Zhang, X. Wang, Y. Shen, S. Zou, H. Qin, K. Sun, J. Hou, W. Shi, C. Li and F. Guo, *Desalination*, 2024, **587**, 117954.

35 C.-G. Liang, A. Yasin, L. Zhang, P. Zhang, K. Zhou, B. Hao, H. Li and P.-C. Ma, *Colloids Surf., A*, 2024, **702**, 135035.

36 Y. Shi, C. Zhang, R. Li, S. Zhuo, Y. Jin, L. Shi, S. Hong, J. Chang, C. Ong and P. Wang, *Environ. Sci. Technol.*, 2018, **52**, 11822–11830.

37 W. Li, Z. Zheng, Z. Qian, H. Liu and X. Wang, *Adv. Funct. Mater.*, 2024, **34**, 2316504.

38 J. VandeVondele, M. Krack, F. Mohamed, M. Parrinello, T. Chassaing and J. Hutter, *Comput. Phys. Commun.*, 2005, **167**, 103–128.

39 T. D. Kuhne, M. Iannuzzi, M. Del Ben, V. V. Rybkin, P. Seewald, F. Stein, T. Laino, R. Z. Khaliullin, O. Schutt, F. Schiffmann, D. Golze, J. Wilhelm, S. Chulkov, M. H. Bani-Hashemian, V. Weber, U. Borstnik, M. Taillefumier, A. S. Jakobovits, A. Lazzaro, H. Pabst, T. Muller, R. Schade, M. Guidon, S. Andermatt, N. Holmberg, G. K. Schenter, A. Hehn, A. Bussy, F. Belleflamme, G. Tabacchi, A. Gloss, M. Lass, I. Bethune, C. J. Mundy, C. Plessl, M. Watkins, J. Vande Vondele, M. Krack and J. Hutter, *J. Chem. Phys.*, 2020, **152**, 194103.

40 J. P. Perdew, K. Burke and M. Ernzerhof, *Phys. Rev. Lett.*, 1996, **77**, 3865–3868.

41 G. Lippert, J. Hutter and M. Parrinello, *Mol. Phys.*, 1997, **92**, 477–488.